PHYSICAL REVIEW B **75**, 155438 (2007)

Interpretation of STM images of graphite with an atomic vacancy via density-functional calculations of electronic structure

Yves Ferro* and Alain Allouche

Laboratoire de Physique des Interactions Ioniques et Moléculaires, Université de Provence/CNRS-UMR 6633, Campus de Saint Jérôme, Services 242 13397 Marseille Cedex 20, France

(Received 12 June 2006; revised manuscript received 20 October 2006; published 30 April 2007)

This paper is devoted to the interpretation of scanning tunneling microscopy (STM) images of a single atomic vacancy on single and double graphene sheets as a model for the (0001) surface of graphite. We first selected a one-layer model which would allow us to run periodic density-functional theory calculations without destroying the charge density waves that form in the vicinity of the vacancy. We assigned the main features of STM images [bright spots in the vicinity of the defect, $(\sqrt{3}\times\sqrt{3})R30°$ modulation of the local electronic density near the Fermi level, third-order symmetry structure] to the electronic band structure of the defective graphite surface. We further analyzed a more extended crystal working cell model to ensure convergence toward the isolated atomic vacancy. The interlayer interaction plays a crucial role in the interpretation of STM images. A double-layer model was subsequently considered and the impact of the interlayer interaction analyzed. We produce the local density of state for the α and β vacancies which may be differentiated. Our calculations reproduce the main features of STM images and the results we get are in good agreement with experimental observations.

DOI: 10.1103/PhysRevB.75.155438 PACS number(s): 73.20.At, 73.20.Hb, 71.15.Mb

I. INTRODUCTION

Surface defects cause long-range modifications on the local electronic structure of graphite.[1–4] Known as Friedel oscillations on metal surfaces,[5,6] they develop as standing waves on the electronic density, spanning regions up to 10 nm from the defects. Scanning tunneling microscopy (STM) makes it possible to directly investigate the electronic features induced by defects with atomic resolution. Tersoff and Hamann[7] have showed that under reasonable approximation, the STM topography is a map of constant charge density at E_F (ρ_{STM}). Therefore, the interpretation of STM images is related to the knowledge of the electronic structure of the graphite surface. Many papers have been presented in this rather busy field of research. One may quote Refs. 1–4, 8, and 9 for atomic vacancies, Refs. 10 and 11 for extended defects such as step edges, Ref. 12 for grain boundary, and Ref. 13 for other extended defects.

Carbon nanotubes and nanoscience are related areas of interest. Extensive literature is also available on the formation of standing waves in nanotubes where the end of the tube as well as the chiral vector define boundary conditions.[14–18]

STM images of perfect graphite surface show a substantial asymmetry between A atoms (over another carbon atom) and B atoms (over the center of an hexagon).[19] Tomanek *et al.*[20,21] have explained this asymmetry as a consequence of the interlayer interactions on the basis of electronic considerations. While the interlayer interaction plays a significant role in STM images, it is usually neglected to model the perturbation created by a single defect on the graphite surface.[4,9] Only Kelly *et al.*[3] have attempted to investigate it with a calculation based on tight-binding theory.

From an experimental point of view, STM images of defective graphite surfaces show a $(\sqrt{3}\times\sqrt{3})R30°$ modulation of ρ_{STM} which is extended over many Å, bright spots in the close vicinity of the vacancy and a third-order symmetry structure;[1–3,22] this last feature looks like a three-branch star. Most of the previous work attempted to interpret these modulations based on electronic considerations (i.e., electronic calculations). However, because of the size of the system needed in order to model the whole perturbation, it was until recently impossible to use the *ab initio* Hartree-Fock (HF) or density-functional theory (DFT) methods. Thus, most of this work was based on tight-binding or Hückel theory methods on single-layer models.[4,1,3] There are nonetheless some studies based on HF and DFT methods. Lee *et al.*[8] attempted the interpretation of STM images in a small 2×2 supercell of two layers in thickness and using an *ab initio* periodic HF full-electron method. Their system was however too small to model the three-branch star structure as well as the $(\sqrt{3}\times\sqrt{3})R30°$ modulation of ρ_{STM}. El-Barbary *et al.*[9] studied the structure and energetic properties of the single vacancy in graphite using DFT on single-layer cluster-type models containing up to 190 carbon atoms. The results from El-Barbary *et al.* provide a good reproduction, at the center of the cluster, of the three-branch star observed at the core of the STM images. However, cluster models are not appropriate to replicate the periodic properties from which the $(\sqrt{3}\times\sqrt{3})R30°$ modulation arises; they suffer from border effects. The end of the π system is truncated on the border of the cluster.

In this paper, we used periodic density-functional theory to analyze the density of states of graphene sheets with a single atomic vacancy. The size of the model to be used is investigated and discussed with regard to the translational symmetry properties of the wave functions. This is a very important point since it determined the feasibility of the calculations. The electronic band structure is plotted along with some relevant square modulus wave functions. The electronic structure is compared with that of a perfect graphene sheet model. The interlayer interaction impact on the electronic properties of the surface is analyzed on a two-layers model with an *AB* stacking. This study aimed to provide a suitable model for the calculation of the electronic properties of graphite near the Fermi level and to assign each component of the STM image to its physical origin: perfect graphite structure, atomic vacancy perturbation, interlayer interaction. Moreover, the shape of the STM images depends on the nature of the probe, tip C_{60} functionalized[3] or tungsten, on the temperature at which the experiment is run,[23] and on the STM bias voltage inducing or not inducing elastic interactions. We supply here some calculated STM images in different domains of energy along with the electronic band structure of the surface to help in the tip-to-surface relationships understanding. We eventually discriminate between α and β sites on the surface, an α site being located just above a carbon atom, a β site above the center of a hexagon ring.

II. METHOD OF CALCULATION

Calculations were performed in the DFT framework using the Perdew, Burke, and Ernzerhof GGA functional for exchange and correlation[24] as implemented in the ABINIT package.[25] The core-valence electron interactions were modeled by means of the Trouiller-Martins pseudopotentials[26] and a plane-waves basis set was used with a cutoff of 25 hartree (680 eV). The occupation was smeared with a Gaussian function with a 0.16 eV full width at full maximum.

The working cells are some $n\times n$ multiple pseudo-two-dimensional (2D) unit cells of one layer in thickness, each layer being separated by a vacuum of 10 Å. Values of n range from 1 to 10. The Brillouin zones associated with each working cell were sampled in order to get an equivalent $36\times36\times1$ $\vec{k}$-point mesh for the Brillouin zone of the unit cell using the Monkhorst-Pack scheme.[27] Thus, the 6×6 working cell was sampled in a $6\times6\times1$ grid of $\vec{k}$ points.

The density of state $\rho(E)$ was computed according to

$$\rho(E) = \frac{2}{V_{\text{cell}}} \sum_{i}^{\text{levels}} \sum_{\vec{k}\in \text{IBZ}} wtk(\vec{k}) g(E - E_i, \sigma_E). \tag{1}$$

Here, $wtk(\vec{k})$ is the weight of the $\vec{k}$ point in the irreducible part of the Brillouin zone (IBZ) and the sum total of all $wtk(\vec{k})$ is normalized to one; $g(E-E_i,\sigma_E)$ is a normalized Gaussian function centered at the energy level E_i. Two different full widths σ_E at full maximum were used: 0.32 eV for the equivalent $36\times36\times1$ $\vec{k}$-point mesh and 0.38 eV for the $3\times3\times1$ grid which were used for the 9×9 and 10×10 working cells. Equation (1) is the density of state (DOS) by definition divided by the volume of the cell. This definition allows us to get the same scale for the many different size models we used.

Applying a small bias voltage V_{bias} between the tip and the sample yields a tunneling current whose density is proportional to ρ_{STM} given by

$$\rho_{\text{STM}}(r, V_{\text{bias}}) = \int_{E_F - eV_{\text{bias}}}^{E_F} \sum_{i}^{\text{levels}} \sum_{\vec{k}\in \text{BZ}} |\varphi_{i,\vec{k}}(\vec{r})|^2 \delta(E_{i,\vec{k}} - E) dE. \tag{2}$$

We have selected an energy domain around the Fermi level: $\Delta E_{\text{STM}}=E_F\pm E$ with $E\approx1$ eV. We then calculated, at the $\vec{k}$ points of the grid, the square modulus of each single electron wave function $\varphi_{i,\vec{k}}(\vec{r})$ whose associated eigenvalues E_i belong to ΔE_{STM}. The band structure was further post-processed solving the Kohn-Sham equation for a series of $\vec{k}$ points along the $\bar{\Gamma}\rightarrow\bar{M}$ and $\bar{\Gamma}\rightarrow\bar{K}$ lines of the BZ. The potential that enters the Kohn-Sham equation was derived from a previous self-consistent calculation, and does not vary during the scan of different k-point lines.

The STM images were calculated according to the Tersoff and Hamann approximation[7] in which the tunneling conductance is proportional to ρ_{STM} given by Eq. (2). Thus, the plots of the many $|\varphi_{i,\vec{k}}(\vec{r})|^2$ and ρ_{STM} are presented as cuts at 3.0 Å and parallel to the graphite layer. The selected domain in energy $\Delta E_{\text{STM}}=[E_F-eV_{\text{bias}};E_F]$ used for the calculation is indicated for each STM image. In addition to ΔE_{STM}, we considered a broadening of 23 meV in order to take into account the distribution of tip electronic states. This broadening is consistent with that of a metal tip at 77 K.

Finally, the Fermi energy was shifted to 0 eV in all the results presented here. Those shifts were applied in order to facilitate comparisons between the results we produced on the different models we used.

III. A SUITABLE WORKING CELL

A. Boundary conditions

Computational time and memory capability limit the size of the system to be used for DFT calculations. The problem is how to choose a suitable unit cell. It should be large enough to avoid cell-cell interactions. It should also be chosen so that the charge density waves (CDW) formed on the vicinity of the vacancy may be established in the model.

The STM probes the local charge density between E_F and E_F-eV_{bias}. All the $\varphi_{i,\vec{k}}(\vec{r})$ belonging to ρ_{STM} are characterized by wave vectors $\vec{k}$ close in norm and direction to $\vec{k}_F$. The wavelength associated to $\vec{k}_F$ is $\lambda_F=3/2a$, where $a=2.45$ Å is the unit-cell parameter of the hexagonal surface cell. Thus, the CDWs in the vicinity of the defect are characterized by $\lambda=3a$ wavelengths and form a $(\sqrt{3}\times\sqrt{3})R30°$ superstructure.[4] We therefore selected a set of working cells whose parameters are $3n\times3n$ that of the surface unit cell. This choice allows for not destroying the CDW formed by one defect inside the working cell. It also allows for not destroying the $(\sqrt{3}\times\sqrt{3})R30°$ modulation of ρ_{STM}.

B. The density of states

In Fig. 1(a) we plotted the band structure of a monolayer of perfect graphite along the high symmetry point of the Brillouin zone shown in Fig. 1(b). In this case, the Fermi surface collapses to a single point at the $\bar{K}$ corner of the BZ.

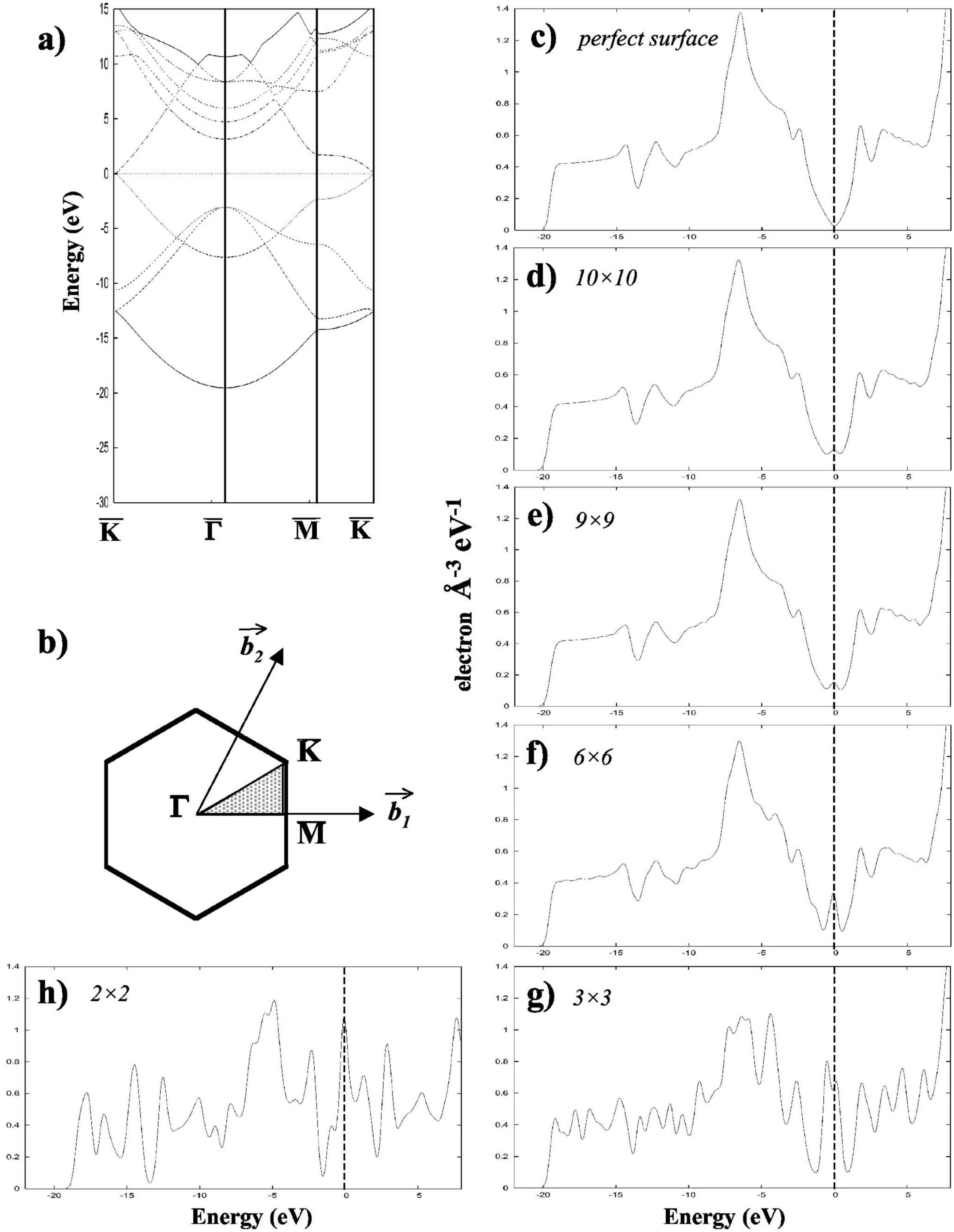

FIG. 1. (a) Band structure of a single layer of graphite plotted following the high-symmetry points of the 2D Brillouin zone shown in (b). Density of states calculated according to Eq. (2) for (c) the perfect surface of graphite and for the (d) 10×10, (e) 9×9, (f) 6×6, (g) 3×3, (h) 2×2 models with an atomic vacancy at the center of the working cells.

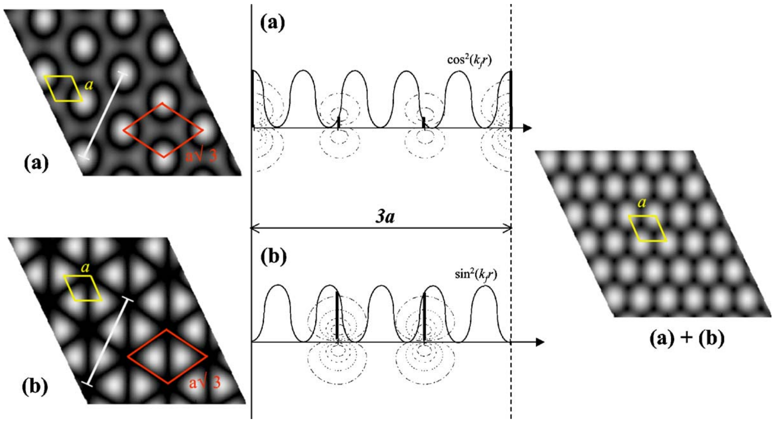

FIG. 2. (Color online) Square modulus of the (a) cosine and (b) sine wave function on A-type atoms, solutions of the Kohn-Sham operator at the Fermi level ($\bar{\Gamma}$ point of the 2D BZ of a 3×3 supercell). (a) and (b) exhibit the $(\sqrt{3}\times\sqrt{3})R30°$ modulation while their sum (a) +(b) have the unit-cell periodicity. $\sin^2(k_f r)$ and $\cos^2(k_f r)$ are also shown and plotted along the white lines shown on the images.

This causes the DOS shown in Fig. 1(c) to vanish at E_F. In Figs. 1(d)–1(h), we plotted the DOS's of the 10×10 to 2×2 models with a vacancy in the center of the working cell. For large working cells, the DOS of graphite remains unperturbed while a localized peak appears at E_F. The DOS then deviates from graphite in both the π and the σ parts as the working cell becomes smaller. The 6×6 working cell is the smallest one to be used as a model for the single vacancy. Below, the graphitic shape of the DOS is destroyed.

A similar investigation was carried out on DOS's of graphite surfaces with vacancies by Hjort *et al.*[28] using the Hückel theory (HT) method on very large clusters. The present results disagree with theirs on several points:

(i) they found a localized peak in the DOS which is associated with vacancies. However, this peak is not centered at E_F and lies just below, which is a crucial point for STM;

(ii) they found that the DOS only weakly deviates from that of perfect graphite, although the concentration of vacancies is as high as 8%. On the contrary, we calculated a DOS for the 3×3 model (5.5% vacancies) which no longer resembles that of graphite.

At this stage, we have defined the conditions to be fulfilled by the model not to destroy the CDW ($3n\times3n$), a minimal size of the system (6×6) to model the single vacancy and a $\vec{k}$-point grid to sample the BZs. Finally, the DOS's we plot show that the vacancy induced local perturbation at E_F, that is in the energy domain of interest for STM.

IV. THE ELECTRONIC STRUCTURE OF GRAPHENE WITH A VACANCY

A. The perfect surface

The observable part by STM of the electronic density comes from wave functions associated to levels located at the $\bar{K}$ corner of the surface BZ where the π and π^* bands connect. At this point, the two independent electronic one-electron wave functions, degenerated solutions of the Kohn-Sham operator, may be written in the LCAO approximation as

$$\varphi_{i,\vec{k}_f}(\vec{r}) = \frac{1}{\sqrt{N}}\sum_{\vec{R}} 2p_Z^{\alpha}(\vec{r}-\vec{R})\exp(i\vec{k}_f\cdot\vec{R}), \qquad \alpha = A,B, \qquad (3)$$

where N is the number of cells imposed by the Born-von Karman boundary conditions we had set and $\vec{R}$ are all the possible translational vectors. A and B refer to the two carbon atoms belonging to the surface unit cell. A-type atoms are located at (0, 0) on the corner of the unit cell and B-type atoms are at $(\frac{1}{3},\frac{2}{3})$. Adding up all $\bar{K}$ solutions of the BZ, we built four degenerated orthogonal electronic one-electron wave functions,

$$\left.\begin{aligned}\varphi_{i,\vec{k}_f}(\vec{r}) &= \frac{2}{\sqrt{N}}\sum_{\vec{R}} 2p_Z^{\alpha}(\vec{r}-\vec{R})\cos(\vec{k}_f\cdot\vec{R}),\\ \varphi_{i,\vec{k}_f}(\vec{r}) &= \frac{2}{\sqrt{N}}\sum_{\vec{R}} 2p_Z^{\alpha}(\vec{r}-\vec{R})\sin(\vec{k}_f\cdot\vec{R}),\end{aligned}\right\} \quad \alpha = A,B. \qquad (4)$$

Within a $3n\times3n$ supercell, the $\bar{K}$ point of the IBZ at $k\,(\frac{1}{3},\frac{1}{3})$ is folded onto the $\bar{\Gamma}$ point at k (0, 0) with a double weight. Thus, the set of two solutions given at the $\bar{K}$ point by Eq. (3) transforms at the $\bar{\Gamma}$ point into that of four solutions given by Eq. (4). In Fig. 2, we plot the square modulus of those solutions for the A atom in a 3×3 supercell model. Each independent solution exhibits the $(\sqrt{3}\times\sqrt{3})R30°$ superstructure while the summation of the sine and cosine square modulus solutions restores the original unit cell (Fig. 2). The same map translated by a $\vec{d}_{AB}$ vector may be found on the B-type atom.

B. The surface with a vacancy

In Fig. 3(a), we plot the band structure close to the Fermi level of a 6×6 model with one A-type site vacant in the center of the working cell. Figure 3(b). shows an enlarged part of this band structure at the $\bar{\Gamma}$ point and near E_F; (m) and (n) are the square modulus of the degenerated solutions of Eq. (4) on B-type atoms at the Fermi level. The (l) solution is 41 meV below E_F; it is the sine solution on A-type atoms with a node on the vacant site. The cosine solution leading to a maximal electronic density on the vacancy does not exist. This result is consistent with the proposals of Mize *et al.*[4] All those three wave functions come from the electronic structure of perfect graphite.

In Fig. 3(b), two degenerate levels (o) and (p) are calculated 10 meV above E_F. As shown on the gray scale images these states are very localized on the vacant site. The dispersion of the electronic band to which they belong is weak,

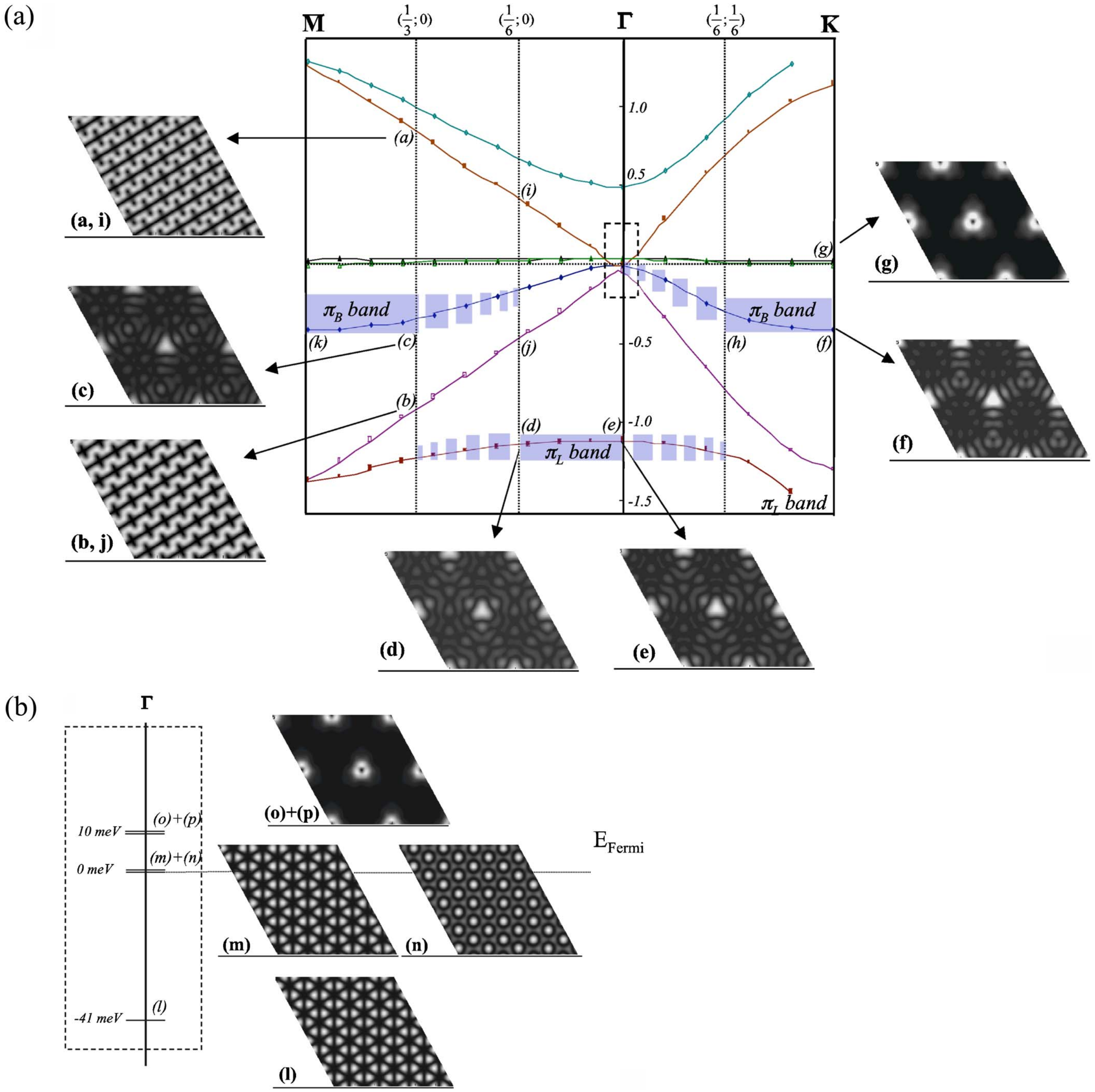

FIG. 3. (Color online) (a) The electronic band structure of the 6×6 model with an atomic vacancy on an A-type site in the center of the working cell. Cuts of the square modulus, shown as the gray scale images, are presented for some relevant point of the band structure from (a) to (k). The three-branch star feature of the π_B and π_L bands are shown as shaded areas. (b) Enlargement of the squared part in (a) at the $\bar{\Gamma}$ point.

$\Delta E = 34$ meV along $\bar{\Gamma}\to\bar{M}\to\bar{K}$. These are local states coming from the defect, and from which the peak at E_F arises in the DOS's of Fig. 1.

The three-branch star pattern is shown in the shaded area in Fig. 3(a). At the $\bar{\Gamma}$ point, the (e) level wave function obtains this pattern. However, this solution is very low in energy (1.14 eV below E_F) and does not belong to ρ_{STM}. Looking at the whole band structure, the three-branch star features jump from this low energy π_L band to the upper π_B band connecting the two degenerated $\sin B(m)$ and $\cos B(n)$ solutions at $\bar{\Gamma}$. The $\vec{k}$-point mesh we used allows us to situate this jump:

(i) between $\left(\frac{1}{6};0\right)$ and $\left(\frac{1}{3};0\right)$ at (c) along the $\bar{\Gamma}\to\bar{M}$ line in Fig. 3(a), that is between −158 meV and −352 meV, respectively,

(ii) and between the $\bar{\Gamma}$ point at (e) and $\left(\frac{1}{6};\frac{1}{6}\right)$ at (h) along the $\bar{\Gamma}\to\bar{K}$ line, between 0 meV and −305 meV.

Thus, within our grid of $\vec{k}$ points, the three-branch star pattern appears between E_F (0 meV) and −305 mV for the 6×6 model.

Finally, we also plotted the square modulus of some other wave functions which exhibit relevant features often observed in STM images of a defective graphite surface.[1]

C. From 6×6 to 9×9 to the isolated vacancy

We ran calculations on the 9×9 model in a looser $3\times3\times1$ grid of $\vec{k}$ points in order to have a trend from the 6×6 model and towards the isolated vacant site. We also compared results from a 6×6 model calculated in some $3\times3\times1$ and $6\times6\times1$ grids of $\vec{k}$ points in order to check that differences do not arise from the different meshes we used. We found the same band dispersions, energy differences from band to band, etc., in both grids. We also found the same pattern of the wave function belonging to the same high symmetry points of the IBZ.

Comparing results from 6×6 to 9×9, we found the following:

(i) In the 9×9 model, the local levels just below E_F remain 10.3 meV above E_F. They are degenerated within 0.8 meV and do not disperse out of a domain of 1.1 meV. We get 21.2 meV and 34.0 meV for the 6×6 model, respectively. The 9×9 model is large enough for these states not to interact from supercell to supercell.

(ii) The sine solution on A-type atoms at $\bar{\Gamma}$ is 155.3 meV, 40.8 meV, and 19.8 meV below E_F for the 3×3, 6×6, and 9×9 models, respectively, that is closer and closer to the Fermi level as the size of the working cell increases.

(iii) The difference in energy between E_F and the upper part of the π_B band having the three-branch star features decreases with increasing working-cell size as shown in Fig. 4. It falls from −352 meV to −270 meV at $\left(\frac{1}{3};0\right)$. We expect this difference to decrease again with larger $3n\times3n$ models until modeling the isolated vacancy.

In Fig. 4, we plotted the local density of states ρ_{STM} for the 6×6 and 9×9 models for different domains in energy. We notice the similarity of the images on both models indicating the working cells we choose to be suitable for modeling a single vacancy. This also indicates a good convergence toward the isolated atomic vacancy.

V. THE INTERLAYER INTERACTION

The interlayer interaction was investigated on a two-layer 6×6 model with graphite sheets separated by 3.35 Å and belonging to an AB stacking; the Brillouin zones were sampled in a $3\times3\times1$ $\vec{k}$-point mesh.

Figures 5(a) and 5(b) show the electronic structures of an atomic vacancy in the double-layer 6×6 model. In both cases, the vacancy belongs to the upper layer. The calculated solutions are plotted at the $\bar{\Gamma}$, $\bar{K}$ and an intermediate point along $\bar{\Gamma}\rightarrow\bar{M}$ at $\left(\frac{1}{3},0\right)$. We thus try to give an idea of the band structure. In the dashed squares, we plotted (i) the $|\varphi_{i,\vec{k}}(\vec{r})|^2$ of Eq. (1) in grey scale at 3.0 Å from the upper layer, (ii) a cut in $|\varphi_{i,\vec{k}}(\vec{r})|^2$ with isocontour lines in a plane perpendicular to the surface and containing A-type atoms, and (iii) the type of solutions (sine, cosine, star feature or local perturbation) for the upper and lower layers into the white square. Grey scale images are always plotted above the upper layer except in Fig. 5(b) where *up* and *down* indicate the considered layer.

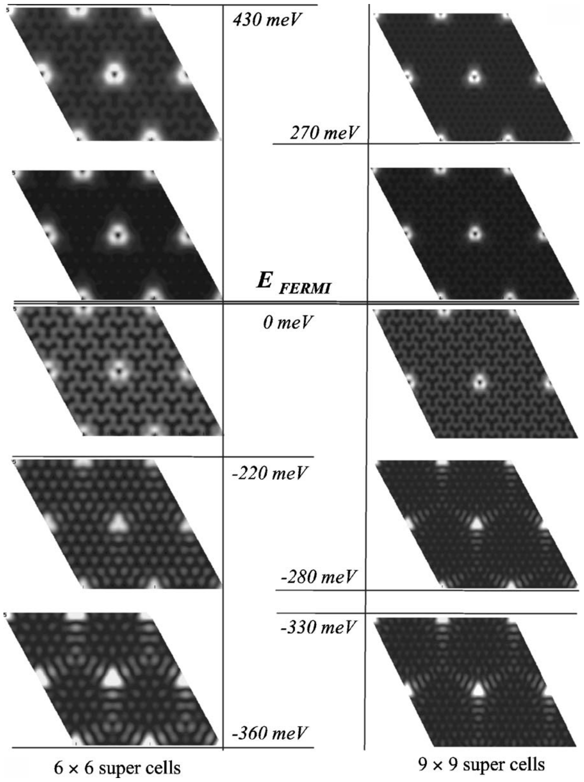

FIG. 4. Calculated STM images for different domain in energy for the 6×6 and 9×9 models.

A. β vacancy

Figure 5(a) shows the electronic structure of a graphite surface where a β vacancy was created by removing a B-type atom on the upper layer of the 6×6 model.

The main results are as follows:

(i) Sine and cosine solutions on A-type atoms split 386 meV above and −288 meV below E_F because of layer-layer bonding and antibonding interactions. A nodal plane at intermediate distance between the upper and lower layer characterizes the antibonding electronic density. On the contrary, some electronic density is created in the same intermediate plane in the bonding case. This splitting brings out the sine and cosine solutions from the Fermi level on A-type atoms.

(ii) Sine solutions on B-type atoms exist separately for the upper and lower layer; this is in line with the absence of interlayer interactions for B-type atoms at the Fermi level. The cosine solution does not exist on the upper layer: it would bring a maximum electronic density in place of the vacancy.[4] The sine solution on the upper layer is 22 meV above E_F at $\bar{\Gamma}$. It is slightly destabilized versus perfect graphite where it appears at E_F. It induces the $(\sqrt{3}\times\sqrt{3})R30°$ superstructure on STM images.

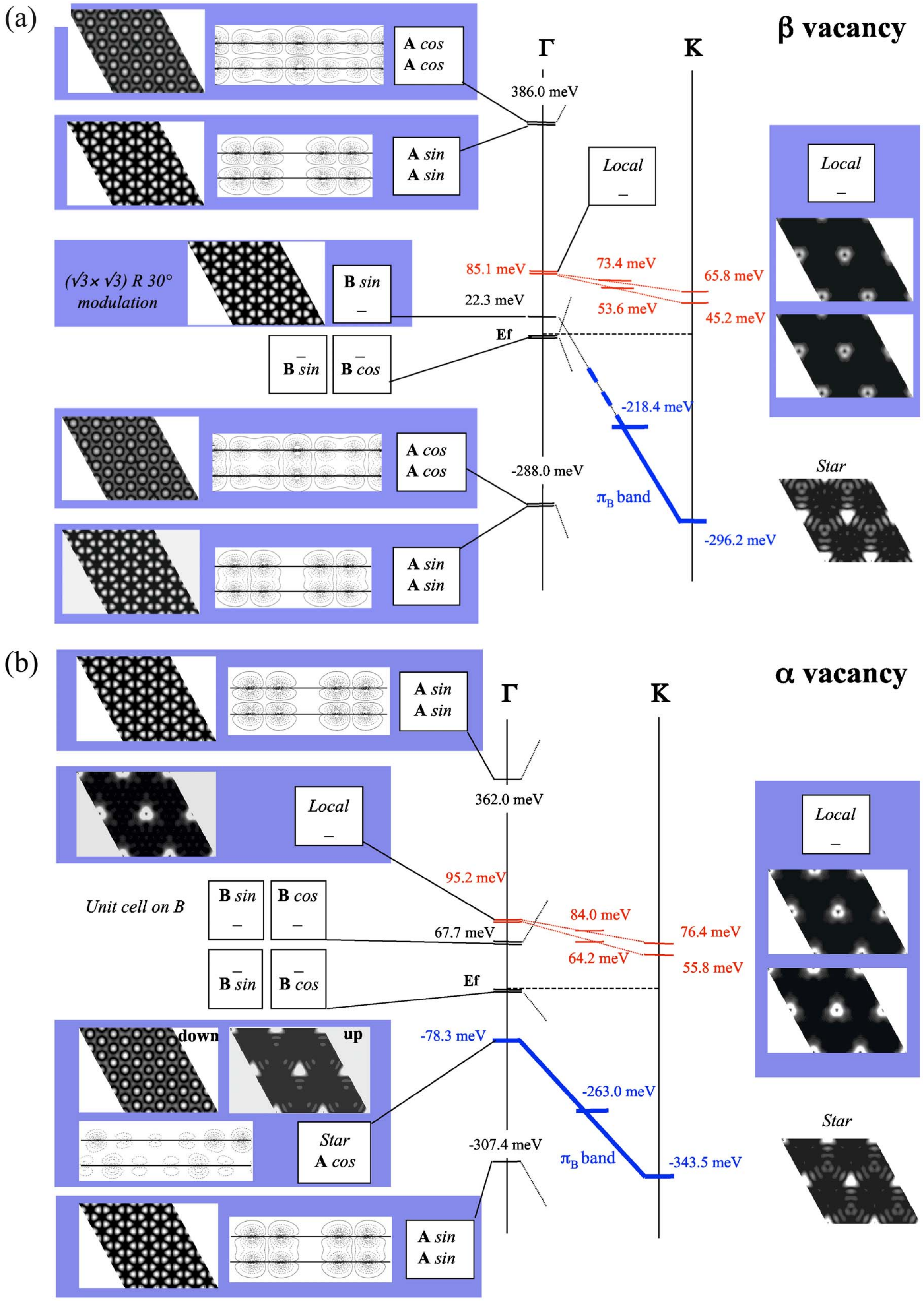

FIG. 5. (Color online) (a) Electronic structures of a β atomic vacancy in the double-layer 6×6 model. Cuts of $|\varphi_{i,\vec{k}}(\vec{r})|^2$ in planes parallel to the surface are plotted in a gray scale, those perpendicular to the surface are plotted as isocontour lines. The three-branch star feature are shown as boldface lines. (b) Electronic structures of an α atomic vacancy in the double-layer 6×6 model. Cuts of $|\varphi_{i,\vec{k}}(\vec{r})|^2$ in planes parallel to the surface are plotted in a gray scale, those perpendicular to the surface are plotted as isocontour lines. The three-branch star feature are shown as boldface lines.

(iii) Local states associated to the vacancy are 85 meV above E_F at $\bar{\Gamma}$. They were only 10 meV above E_F in the monolayer case [Fig. 3(a)]. As in the preceding section, the weak dispersion of these states along $\bar{\Gamma} \rightarrow \bar{K}$ is due to low cell-cell interactions. These states are surface states that only involve atoms from the upper layer.

(iv) The star feature appears on the π_B band connecting the upper sine solution on B-type atoms. It is found at $\bar{K}$ (−296 meV) and at the intermediate point (−218 meV) but not at $\bar{\Gamma}$ as in the monolayer case [Fig. 3(a)].

The main consequence of the interlayer interaction is the splitting of the A-type atoms bringing the corresponding solutions out of ΔE_{STM} and the weaker dispersion of the π_B band making the three-branch star feature appear closer from E_F.

B. α vacancy

In Fig. 5(b), we plotted the electronic structure of an α vacancy created by removing an A-type atom from the upper layer of the 6×6 model.

The main results are as follows:

(i) Sine solutions on A-type atoms also split because of bonding and antibonding interactions. The cosine solution does not exist for A-type atoms on the upper layer. The $(\sqrt{3} \times \sqrt{3})R30°$ modulation thus disappears since the splitting of the sine solutions brings them out of ΔE_{STM}.

(ii) The cosine solution on the lower layer is combined with the star feature solution on the upper layer. Thus, a π_B band having the three-branch star feature exists everywhere in the BZ contrary to what we had found above [Fig. 5(a)] and to the monolayer model [Fig. 3(a)].

(iii) Sine and cosine solutions on B-type atoms exist again separately for the upper and lower layer. Their related energies are 67.7 meV above E_F at $\bar{\Gamma}$. These solutions do not induce a $(\sqrt{3} \times \sqrt{3})R30°$ modulation of ρ_{STM} since the combination of the sine and cosine solutions restores the unit cell on B-type atoms.[4]

(iv) Local states associated to the vacancy are 95.2 meV above E_F and weakly disperse along $\bar{\Gamma} \rightarrow \bar{K}$.

The main consequences of the interlayer interaction are the splitting of the sine solutions on A-type atoms and the presence of the three-branch star feature everywhere in the BZ, and particularly at the $\bar{\Gamma}$ point at an energy (−78.3 meV) very close to E_F.

VI. DISCUSSION

From our results, the main features of the electronic structure of a graphene sheet with vacancy are, at the $\bar{\Gamma}$ point, the presence of

(i) degenerated levels related to sine and cosine solutions on B-type atoms at E_F,

(ii) a single level just 40 meV below E_F maximum and related to the sine solution on the A-type atom.

These levels belong to the unperturbed electronic structure of perfect graphite.

Over the whole IBZ, the main features are

(iii) the presence of localized states roughly 10 meV just above E_F and which do not disperse. These are the local states associated with the defect.

(iv) a π_B band having the three-branch star feature all over the Brillouin zone except around $\bar{\Gamma}$. These levels are perturbations of the π electronic band of graphite.

These main electronic features may be, respectively, connected to the following STM images' main features:

(i) the unit cell still appears in the background while,

(ii) a $(\sqrt{3} \times \sqrt{3})R30°$ modulation is superimposed on the image,

(iii) the presence of bright spots in the neighborhood of the vacancy, and

(iv) the third-order symmetry structure pattern.

These features are indeed observed in the image from Ruffieux *et al.* in Refs. 2 and 1.

The surface relaxation was neglected here because of computational limits. El-Barbary *et al.*[9] were the only ones to investigate this problem on single-layer cluster models. They found a symmetry reduction (from D_{3h} to C_{2v}) but no significant alteration of the shape of ρ_{STM}; the three-branch star feature is slightly distorted, losing its threefold symmetry. Moreover, the electronic structure remains unchanged near the Fermi level except for the two degenerated levels associated to the local perturbation. One of them is raised to high energy while the other remains in the close vicinity (within 40 meV depending on the clusters) of the Fermi level, below the sine and cosine solution of perfect graphite. This implies that no significant modification of the ρ_{STM} we calculated should be expected with surface relaxation. The effect would eventually be to increase the brightness of the local perturbation on the vacancy while scanning the occupied local density of state.

The interlayer interaction was further investigated on a two-layers model. It follows from our results that the electronic structure is not symmetric above and below the Fermi level. The most important result is that the electronic structure is very different near E_F on α and β vacancies. Thus, it should be possible to discriminate between them on STM images, the bilayer system being a model for the (0001) surface of graphite. This is shown in Fig. 6 where we plotted the STM images calculated at different energies for both α and β vacancies.

The major difference is induced, on the β vacancy. At $\bar{\Gamma}$, the sin B solution induces a $(\sqrt{3} \times \sqrt{3})R30°$ modulation over the whole domain in energy we considered, on the contrary with the α vacancy. The three-branch star feature appears at low energy along the band connecting the sin B solution [Fig. 5(a)]. As for the monolayer, we defined a domain in energy [22.3;−218.4] meV in which it appears. A finer grid of $\vec{k}$ points would be necessary to better define it. In the α vacancies case, the three-branch star feature exists since 78.3 meV below E_F and is apparent along the whole band from $\bar{\Gamma}$ to $\bar{K}$ [Fig. 5(b)]. Considering the broadening due to the tip electronic distribution, this feature may appear at weak energy starting from −55 meV. This result is in very good agreement with the findings of Ruffieux *et al.*[2,1] who observed this pattern for bias voltage of 36 mV and 70 mV, respectively.

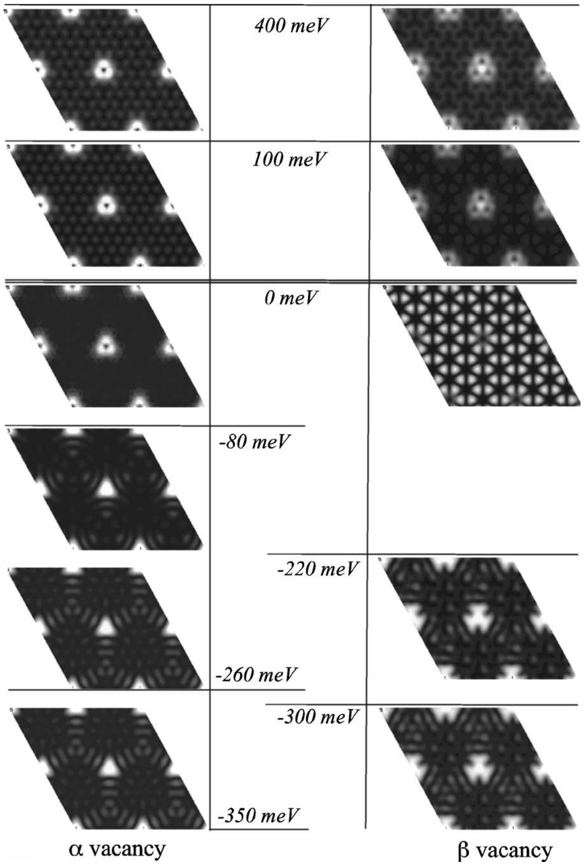

FIG. 6. Calculated STM images for different domains in energy for the α and β vacancies.

Kelly *et al.*[3] using a tight-binding model have calculated STM images for α and β vacancies. This method allows investigating larger models. However, it does put limits on the investigation of the π system (subject to empirical parameters) and does not take into account quantum effects as exchange and correlation unlike the DFT method we used. Kelly *et al.*[3] found the three-branch star to be rotated by 60° from α to β vacancy. This result we reproduced (Fig. 6) was indeed observed from an experimental point of view by Kushmerick *et al.*[23]

The $(\sqrt{3}\times\sqrt{3})R30°$ modulation is only present around a β vacancy (Fig. 6). Thus, above E_F, STM images are consistent with the local perturbation plus this modulation. On α vacancies, it consists of the local perturbation plus the pattern of the unit cell in the background. This is consistent with the results from Hahn *et al.*[29,22] who observed similar images as those we found on an α vacancy at 100 meV with bias voltage of −36 and −60 mV (36 and 60 meV above E_F).

VII. CONCLUSION

The models we built allowed us to calculate, within the DFT framework, the electronic structure of graphene and graphite bilayers with vacancies. We assign each main feature of STM images to some main features of the electronic structure of the surface near the Fermi level. The impact of the interlayer interaction was further investigated. It splits the solution above and below the Fermi level for the solutions involving the A-type atoms. On α vacancies, this causes the $(\sqrt{3}\times\sqrt{3})R30°$ modulation based on A atoms to disappear while the three-branch star feature comes closer to the Fermi level. On the contrary, on a β vacancy, ρ_{STM} is dominated by the $(\sqrt{3}\times\sqrt{3})R30°$ modulation based on B-type atoms while the unit-cell network based on A atoms is moved away from E_F. In both cases, the local surface states with a high-density region centered on the defect are almost unaffected. Those results are in good agreement with experimental observation and allow differentiating α and β atomic vacancy on a graphite surface.

ACKNOWLEDGMENTS

The authors would like to thank J.-P. Legré and T. Angot for constructive discussions. This work is supported by the Euratom-CEA association in the framework of the LRC (Laboratoire de Recherche Conventionnée CEA/DSM-Université de Provence PIIM).

---

*Electronic address: yves.ferro@up.univ-mrs.fr

[1] P. Ruffieux, M. Melle-Franco, O. Gröning, M. Bielmann, F. Zerbetto, and P. Gröning, Phys. Rev. B **71**, 153403 (2005).
[2] P. Ruffieux, O. Gröning, P. Scwaller, L. Schlapbach, and P. Gröning, Phys. Rev. Lett. **84**, 4910 (2000).
[3] K. F. Kelly and N. J. Halas, Surf. Sci. **416**, L1085 (1998).
[4] H. A. Mizes and J. S. Foster, Science **244**, 559 (1989).
[5] J. Repp, F. Moresco, G. Meyer, K. Rieder, P. Hildgard, and M. Persson, Phys. Rev. Lett. **85**, 2981 (2000).
[6] P. T. Sprunger, L. Petersen, E. W. Plummer, E. Lægsgaard, and F. Besenbacher, Science **275**, 1764 (1997).
[7] J. Tersoff and D. R. Haman, Phys. Rev. B **31**, 805 (1985).
[8] K. H. Lee, M. Causá, S. S. Park, C. Lee, Y. Suh, H. M. Eun, and D. Kim, J. Mol. Struct.: THEOCHEM **506**, 297 (2000).
[9] El-Barbary, R. H. Telling, C. P. Ewels, M. I. Heggie, and P. R. Briddon, Phys. Rev. B **68**, 144107 (2003).
[10] Y. Niimi, T. Matsui, H. Kambara, K. Tagami, M. Tsukada, and H. Fukuyama, Phys. Rev. B **73**, 085421 (2006).
[11] Y. Kobayashi, K. Fukui, T. Enoki, K. Kusabe, and Y. Kaburagi, Phys. Rev. B **71**, 193406 (2005).
[12] P. Simonis, C. Goffaux, P. A. Thiry, L. P. Biro, Ph. Lambin, and V. Meunier, Surf. Sci. **511**, 319 (2002).
[13] N. Takeuchi, J. Valenzuela-Benavides, and L. Morales de la Garza, Surf. Sci. **380**, 190 (1997).
[14] Z. Osváth, G. Vértesy, L. Tapasztó, F. Wéber, Z. E. Horváth, J. Gyulai, and L. P. Biró, Phys. Rev. B **72**, 045429 (2005).
[15] V. Meunier and Ph. Lambin, Phys. Rev. Lett. **81**, 5588 (1998).
[16] C. L. Kane and E. J. Mele, Phys. Rev. B **59**, R12759 (1999).
[17] A. Rubbio, D. Sanchez-Portal, E. Artacho, P. Ordejón, and José M. Soler, Phys. Rev. Lett. **82**, 3520 (1999).

[18] S. G. Lemay, J. W. Janssen, M. van den Hout, M. Mooij, M. J. Bronikowski, P. A. Willis, R. E. Smalley, L. P. Kouwenhoven, and C. Dekker, Nature (London) **412**, 617 (2001).

[19] W. T. Pong and C. Dukan, J. Phys. D **38**, R329 (2005).

[20] D. Tomanek, S. G. Louie, H. J. Mamin, and D. W. Abraham, Phys. Rev. B **35**, 7790 (1987).

[21] D. Tomanek and S. G. Louie, Phys. Rev. B **37**, 8327 (1988).

[22] J. R. Hahn and H. Kang, Phys. Rev. B **60**, 6007 (1999).

[23] J. G. Kushmerick, K. F. Kelly, H. P. Rust, N. J. Halas, and P. S. Weiss, J. Phys. Chem. B **103**, 1619 (1999).

[24] J. P. Perdew, K. Burke, and M. Ernzerhof, Phys. Rev. Lett. **77**, 3865 (1996).

[25] ABINIT http://www.abinit.org

[26] N. K. Trouiller and J. L. Martins, Phys. Rev. B **43**, 1993 (1991).

[27] H. J. Monkhorst and J. D. Pack, Phys. Rev. B **13**, 5188 (1972).

[28] M. Hojrt and S. Stafström, Phys. Rev. B **61**, 14089 (2000).

[29] J. R. Hahn, H. Kang, S. Song, and I. C. Jeon, Phys. Rev. B **53**, R1725 (1996).